Available online at www.sciencedirect.com

SciVerse ScienceDirect

Acta Materialia 61 (2013) 2531–2547

Acta MATERIALIA

www.elsevier.com/locate/actamat

Modeling fatigue crack growth resistance of nanocrystalline alloys

Piyas B. Chowdhury [a], Huseyin Sehitoglu [a,*], Richard G. Rateick [b], Hans J. Maier [c]

[a] Department of Mechanical Science and Engineering, University of Illinois at Urbana-Champaign, 1206 West Green Street, Urbana, IL 61801, USA
[b] Honeywell Aerospace, 3520 Westmoor Street, South Bend, IN 46628, USA
[c] Institut für Werkstoffkunde (Materials Science), Leibniz Universität Hannover, D-30823 Garbsen, Germany

Received 18 November 2012; received in revised form 16 January 2013; accepted 17 January 2013
Available online 15 February 2013

Abstract

The description of fatigue crack growth in metals has remained an empirical field. To address the physical processes contributing to crack advance a model for fatigue crack growth (FCG) has been developed utilizing a combined atomistic–continuum approach. In particular, the model addresses the important topic of the role of nanoscale coherent twin boundaries (CTB) on FCG. We make the central observation that FCG is governed by the dislocation glide resistance and the irreversibility of crack tip displacement, both influenced by the presence of CTBs. The energy barriers for dislocation slip under cyclical conditions are calculated as the glide dislocation approaches a twin boundary and reacts with the CTB. The atomistically calculated energy barriers provide input to a mechanics model for dislocations gliding in a forward and reverse manner. This approach allows the irreversibility of displacement at the crack tip, defined as the difference between forward and reverse flow, to be determined. The simulation results demonstrate that for both refinement of twin thickness and a decrease in crack tip to twin spacing FCG resistance improves, in agreement with recent experimental findings reported in the literature.

Keywords: Fatigue; Nanocrystalline; Nickel; Damage tolerance; Coherent twin

1. Introduction

Current assessment of materials for damage tolerance is based on methodologies that were developed more than 40 years ago. These methodologies are empirical and "rule based", such as the well known ASME Design Code [1] that treats combined fatigue and creep damage. Today it remains a challenge to predict material degradation under fatigue loading conditions utilizing scientific principles. Compared with unidirectional deformation, fatigue introduces irreversibilities that are characteristic of cyclical deformation. These irreversibilities are a strong function of the crystal structure, the alloy composition, and the interface interactions. Nanocrystalline materials with twin boundaries [2–10] have attracted considerable attention recently, and possess combined strengthening attributes with higher ductility. On the other hand, their fatigue damage tolerance characteristics have received less consideration, and the present paper is geared towards building a framework for the modeling of fatigue crack growth in nanomaterials.

A number of studies have elucidated the strengthening mechanisms in nanocrystalline materials under monotonic loading conditions [2–4,11–15]. Fatigue studies of nanocrystalline metals displaying higher endurance limits [16–20] compared with their coarse grained counterparts have also been undertaken. Recent works have also demonstrated superior damage tolerance [5,21] in the presence of nanoscale twins, hence the prospect of enhanced overall fatigue resistance with combined monotonic strength holds considerable promise. In particular, Singh et al. [5] demonstrated that introducing nanotwins with a gradually diminishing lamellar spacing in ultrafine grained (UFG) Cu substantially improved damage tolerance metrics such as the threshold stress intensity range ΔK_{th} and, most significantly, the

* Corresponding author.
E-mail address: huseyin@illinois.edu (H. Sehitoglu).

1359-6454/$36.00
http://dx.doi.org/10.1016/j.actamat.2013.01.030

near-threshold crack growth rate da/dN. Moreover, studies by Sangid et al. [21] on electro-deposited nanocrystalline nickel–cobalt alloys with a high volume fraction of annealing twins in the grains further corroborated the existence of superior fatigue crack growth (FCG) impedance. While these studies point to the significance of coherent boundaries on FCG behavior, understanding the mechanistic origin of such microstructure-driven phenomena necessitates a detailed study informed by the underlying atomistics, capturing the operative cyclical crack tip plasticity at the appropriate length scale. The current paper has developed a model for subcritical FCG behavior combining atomistic and continuum considerations in the presence of twin lamellae of nanoscale thickness and spacing. The advantage of the model is that there are no adjustable parameters (fitting constants) and crack propagation occurs due to the irreversibility of plastic flow at crack tips.

A fatigue crack advances because of the irreversible glide of dislocations emitted by the crack-tip, the degree of which dictates the net plastic displacement per cycle [22–30]. Pippan et al. [27–29] showed that crack tip displacement under forward and reverse loading does not cancel out because of dislocation annihilation, resulting in fatigue crack advance. We note that microstructural factors that would influence the degree of glide irreversibility must also alter the FCG rates. Specifically, microstructural obstacles, such as coherent twin boundaries (CTBs) and grain boundaries (GBs), in the neighborhood of an advancing crack mean that the slip reversibility is difficult to ascertain. The extent of irreversibility imposed by these obstacles is a function of the nature of the slip–interface interactions. At the same time, the presence of such interfaces influences the resistance to slip propagation τ_o (i.e. the difficulty of plastic flow advancing past the obstacle, manifested as an elevation of the unstable fault energy γ_{us}). γ_{us} is the maximum fault energy during slip established from the block-like motion of an upper surface relative to a lower one. Inevitably, its extrinsic (modified) level will change due to the intersection of slip with interfaces. The resulting crack growth rate da/dN is related to the slip paths, residual dislocations, and conservation of the Burgers vectors as influenced by the twin width and spacing.

Fig. 1 depicts the forward slip emission from an advancing fatigue crack and its interaction with a CTB. The nature of the slip–CTB interaction is a function of the type of incident dislocation (pure edge, pure screw or mixed). Residual dislocations with a total Burgers vector b_r are an outcome of these reactions, which depend on the interface orientation and the resolved shear stresses of the incoming and outgoing slip systems [31,32]. Variations in such slip–twin reactions would ultimately modify the glide path irreversibility. The fatigue crack growth resistance is expected to change with the four factors shown in Fig. 1, the irreversibility (denoted p), the intrinsic stress τ_o related to the gamma surface (Generalized Stacking Fault Energy), and the twin thickness t and twin spacing d. If the irreversibility p is 0 no crack growth can occur. We show that the irreversibility is dictated by the gamma surface differential upon forward and reverse flow at the crack tip.

The prevalence of twins, as in the case of the Ni–Co alloy seen in the transmission electron microscopy (TEM)

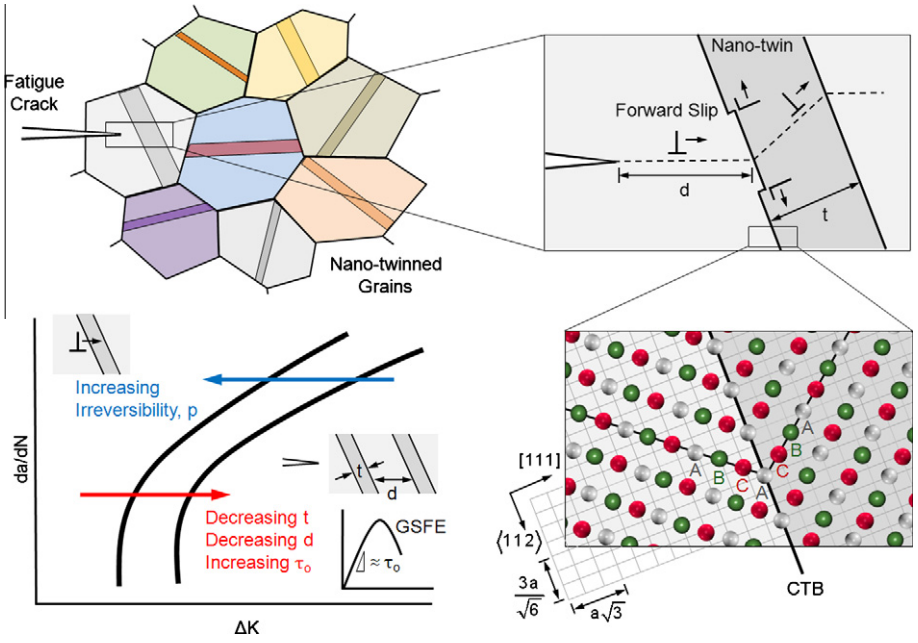

Fig. 1. Schematics representing the focus of the investigation in this paper. In forward load an advancing fatigue crack emits dislocations (pure screw type under mode III loading) which interact with a nanoscale twin. Slip-coherent twin boundary (CTB) interactions dictate the FCG mechanism. The current work studied the isolated role of twin lamellae width (t) and the crack to twin spacing (d) on the FCG behavior in a single nanotwinned grain. The coherency of the twin boundaries allows glissile motion of dislocations on the CTB, unlike incoherent GB. Factors that influence fatigue crack growth behavior are summarized. In addition to t and d, the glide strength, τ_0 and the irreversibility, p, under cyclical loading influence fatigue crack growth rates.

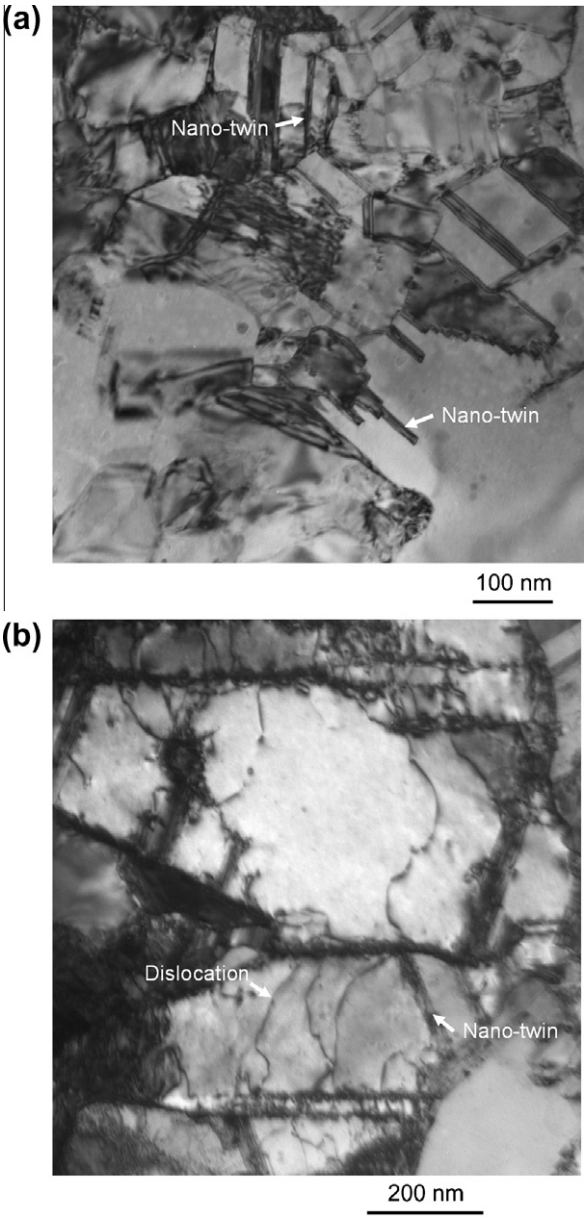

Fig. 2. (a) TEM images of Ni–1.62 wt.% Co alloy before the fatigue experiment. Notice the prevalence of nanotwins. (b) Post-fatigue TEM images of Ni–1.62 wt.% Co alloy. A high degree of slip–twin/GB interaction is noticeable.

image of a pre-FCG experimental specimen (Fig. 2a), improves the FCG resistance to a considerable degree. Fig. 2b demonstrates an enhanced degree of dislocation pile-up at twin boundaries and GBs, indicating slip-mediated crack tip plasticity as the primary deformation mechanism. Intuitively, the implied improvement in FCG [5,21] points to a special mechanism(s) involved in cyclical slip–CTB interactions. Hence, one needs to establish the underlying governing physics that decide dislocation glide, which is susceptible to local stress sources (e.g. GB, CTB, residual sessile dislocations).

The dislocation gliding mechanism depends on the dislocation core properties. Glissile motion occurs by alternately rearranging atomic distortion that proceeds via successive tearing and forming of atomic bonds surrounding the core structure [33]. The driving shear stress for such motion scales with the activation energy barriers for the translational motion onto a close-packed slip plane. The energetics of dislocation translation lie in the relative motions of the core atoms. Alteration of the dislocation gliding condition, as influenced by nano-obstacles and the respective energetics, necessitates a non-continuum modeling framework. In that regard, molecular dynamics (MD) allows the capture and quantification of the physics of slipping at the atomistic length scale. MD simulates the time evolution of atomic nuclei (considered as classical Newtonian particles) by integrating their equations of motion [34]. The metallic bonding is modeled through a homogeneously distributed electron cloud functional and a pairwise interaction potential. A semi-empirical embedded atom method (EAM) formalism, curve fitted with experimental and/or ab initio material properties, employs such modeling to accurately describe the bonding energy landscape [35]. Utilizing MD simulations with an EAM potential Ezaz et al. [31] quantified the energetics of dislocation glide upon interaction with twins under monotonic conditions. In the literature some researchers [36–38] have employed MD-EAM methods to study massive cyclical slip emissions leading to nanovoid coalescence as the crack advancing mechanism in the presence of GBs. However, the physics of slip irreversibility accumulation, as the underlying incentive for crack tip plasticity, has not yet been explored.

In our approach we employ atomistic simulations to reveal the nature of slip–twin interaction under cyclical conditions, and the underlying fault energy barriers. Such a perspective reveals the exact role of CTBs as irreversibility-inducing microstructural elements as well as effective barriers to cyclic slip. Quantification of the cyclical slip–twin reaction energetics allows the calculation of ideal shear stresses for to and fro glide, as modified by the presence of CTBs and/or residual dislocations. We incorporate these atomistically extracted material properties in fracture mechanics-based formulations to simulate FCG undergoing large scale slip activities. The mechanics simulations employ cyclical irreversibility as the principal driving force of crack advancement in the presence of nanotwins. The combination of two different length scale methodologies is important, in that the continuum descriptions of FCG utilize input from the governing atomistic physics. Hence we obtain an in-depth understanding of FCG as influenced by nanotwins. Such an insight highlights the role of some critical characteristic dimensions associated with these nano-obstacles (e.g. twin lamellar thickness and twin to crack tip spacing) on the FCG metrics.

2. Methods

To develop a FCG methodology we employed both atomistic slip-twin and fracture mechanics-based crack-tip

slip simulations. An open source software LAMMPS (large-scale atomic/molecular massively parallel simulator) [39] was used to perform the MD simulations. A semi-infinite discrete dislocation simulation set-up was then established using input from the MD results. The combination of these simulations provides a convenient conduit to explore some fundamental aspects of the mechanism of FCG.

For the MD simulations a nickel single crystal grain was constructed with the crystallographic orientation shown in the inset in Fig. 3. This grain contains a coherent twin of finite thickness. A stress concentrator (atom size void) placed in the matrix simulates a dislocation source. The whole system was energetically minimized, using the conjugate gradient (CG) algorithm [34]. This resulted in an energetically stable single nanotwinned grain. The CG algorithm iteratively solves atomic coordinates to reach the minimum energy of the system within a predefined convergence limit. An acceptance criterion adjusts the new atomic positions, conjugate to the previous ones that follow the direction of steepest descent on the potential energy curve. Moreover, enforcement of three-dimensional periodic boundary conditions on the supercell eliminates the effects of free surface energy, thereby simulating a system of bulk material. The supercell dimensions were configured such that the physical observables (e.g. temperature, pressure, kinetics and potential energy of the system) converged to system size independence. In view of the goals of the present work we conducted a number of MD simulations with varying source to twin distances as well as twin lamellar widths. Consequently, the supercell size was varied accordingly to give the optimally converged dimensions for each simulation, avoiding any artifacts of periodicity.

Cyclical shear was applied to the supercell under strain control conditions. A strain range of $\varepsilon_{min} = -4.46\%$ to $\varepsilon_{max} = 9.22\%$ (i.e. $R_\varepsilon = -0.48$) was selected to facilitate slip nucleation from the void (slip source), and sufficient plastic flow to provide to and fro glissile motion across the twin. The MD simulations were run for a duration of several hundred picoseconds. Such a timescale is inherent in MD simulations, limited by the computational capability. Our investigation required the calculation of parameters such as the local plastic shear strain due to slip, the Burgers vectors thereof, and the energetics of slip–twin reactions. These parameters are unaffected by the high deformation rates arising from such a timescale. In order to conduct non-equilibrium MD simulations (i.e. evolution of the system under the imposed conditions) we employed an isobaric–isothermal (NPT) ensemble along with a Nosé–Hoover thermostat algorithm. Hence, the total number of atoms N, the external pressure P, and the temperature T (at 10 K) of the system were held constant. The dynamics of deformation proceeded utilizing the velocity Verlet algorithm as the time integrator. Atomistic snapshots at different time points were carefully analyzed using visual molecular dynamics (VMD) [40] and AtomEye configuration viewer [41]. These visualization tools, combined with in-house MATLAB programs, helped capture the details of slip–twin interactions (e.g. the conservation of Burgers vectors) and calculate fault energies, glide distance of slip, etc. Volume-averaged virial stress formulation, neglecting the kinetic energy contribution [42], was employed in order to quantitatively assess the stress–strain response of the system.

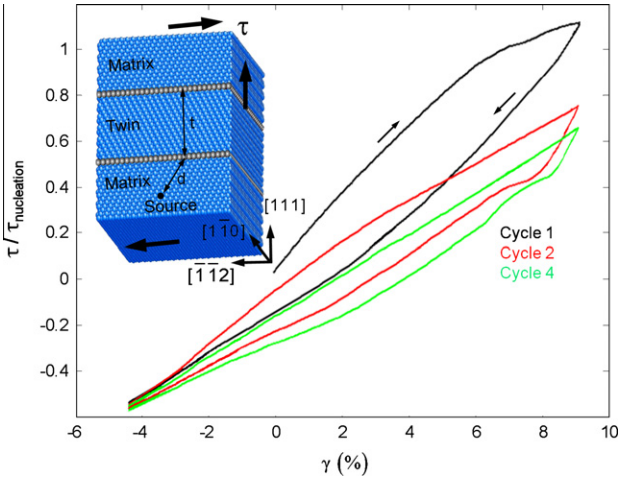

Fig. 3. Cyclical stress–strain response of a nanotwinned grain with a dislocation source (not shown) in the matrix in the vicinity of the coherent twin boundary as obtained by MD simulations. The configuration above produces pure screw dislocations.

One essential part of our investigation was to calculate the energetics of complex cyclical slip–twin reactions, necessitating accurate descriptions of the atomic level energy landscape through EAM formulations [35]. A comparative study of EAM potentials available in the literature demonstrated that the Foiles and Hoyt potential [43] provides good agreement between the unstable fault energy γ_{us}, the density functional theory (DFT) calculations (254 mJ m^{-2}), and the intrinsic stacking fault energy (γ_{isf}) with the experimental finding (127 mJ m^{-2}). The interplanar potential energy profiling incorporating all of these parameters is termed the generalized stacking fault energy (GSFE) curve [44], as shown in Fig. 6. The GSFE represents the energy pathway to create the lattice distortion of a dislocation along the Burgers vector direction. A typical GSFE is calculated by sliding one crystalline half-space on top of another on the slip plane along the slip direction. We utilized the Foiles and Hoyt EAM potential to compute the modified GSFE, as influenced by local stresses during back and forth dislocation glide traversing the twin (to be discussed in detail later). For a more thorough description of the MD simulation procedures employed in the present work readers are referred to Ezaz et al. [31].

3. Results

3.1. Molecular dynamics simulations

Fig. 3 shows a typical MD-based cyclical shear stress–strain response of a nanotwinned grain with a dislocation

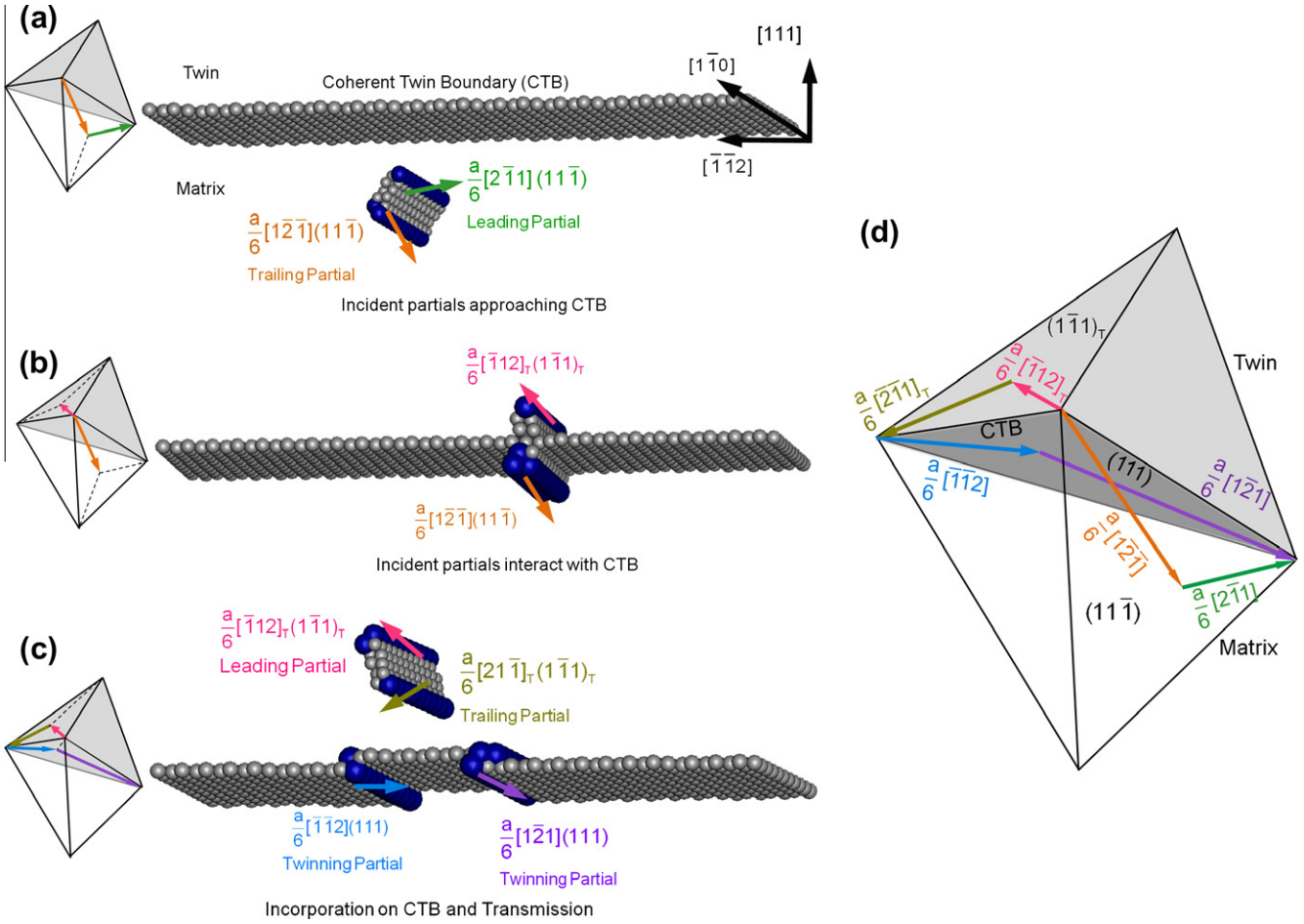

Fig. 4. (a) Steady-state cyclical slip–twin interaction for the forward part of a MD fatigue cycle (for visualization convenience perfect lattice atoms are rendered invisible and only defect atoms are shown). The dissociated leading and trailing partials emitted from the source (not shown) are approaching the closest CTB. All vectors (in the matrix and/or twin) are represented in their respective coordinate frames. (b) Two partials recombining upon interacting with a CTB. The emerging leading Shockley partial (pink) and incident trailing Shockley partial (brown) are shown. The situation shown depicts the metastable phase of the slip–twin reactions. More dislocations subsequently nucleate. (c) Nucleation of multiple dislocations as a result of the incident dislocation–CTB interaction. (d) A simplified double Thompson tetrahedron depiction of the dislocation reactions during forward flow at a CTB depicting conservation of the Burgers vectors. (For interpretation of the references to colour in this figure legend, the reader is referred to the web version of this article.)

source located in the matrix. Cyclical deformation is applied to the extent that it facilitates dislocation nucleation, and with a sufficient degree of slip to intersect the twin, located at a distance d from the source. The strain range for subsequent cyclical loading is set up such that to and fro dislocation motions occur across the width t of the twin. Separate MD simulations were carried out with varying finite twin lamellar widths and crack to twin spacings to study the influences of these dimensions. With a gradual increase in t or d the external loading needs to be increased in order for the slip to reach and traverse the entire width of the nanotwin. Consequently, a gradually greater number of dislocations nucleate with the increase in the applied load. The multitudes of dislocations undergo relatively more complex forms of interactions with the CTBs at larger t and/or d. Nevertheless, we observed a generalized pattern of cyclical slip–twin interaction with simultaneous incorporation and transmission of slip for all cases of varying t and/or d. Hence the fundamental similarities reside in the type of interaction and the introduction of irreversible slip activity in each cycle, irrespective of the number of incident dislocations. In the following section the cyclical slip–twin reaction involving only one incident dislocation (pure screw type) is described in detail for the case of smaller t and d (requiring a lower applied load).

As can be seen in Fig. 3, the stress–strain approaches a saturated response as the cyclical slip–twin interaction mechanism also achieves a recurrent steady-state. Since the MD simulations were performed on pristine crystals, and at high deformation rates, the stresses from the MD are high compared with the experimental stress–strain response. However, the dislocation reactions associated with the slip–twin interactions are unaffected, as verified by running simulations at different strain rates. Therefore, the cyclical stress–strain plots in Fig. 3 are interpreted only to obtain a quantitative estimation of the quasi-steady-state

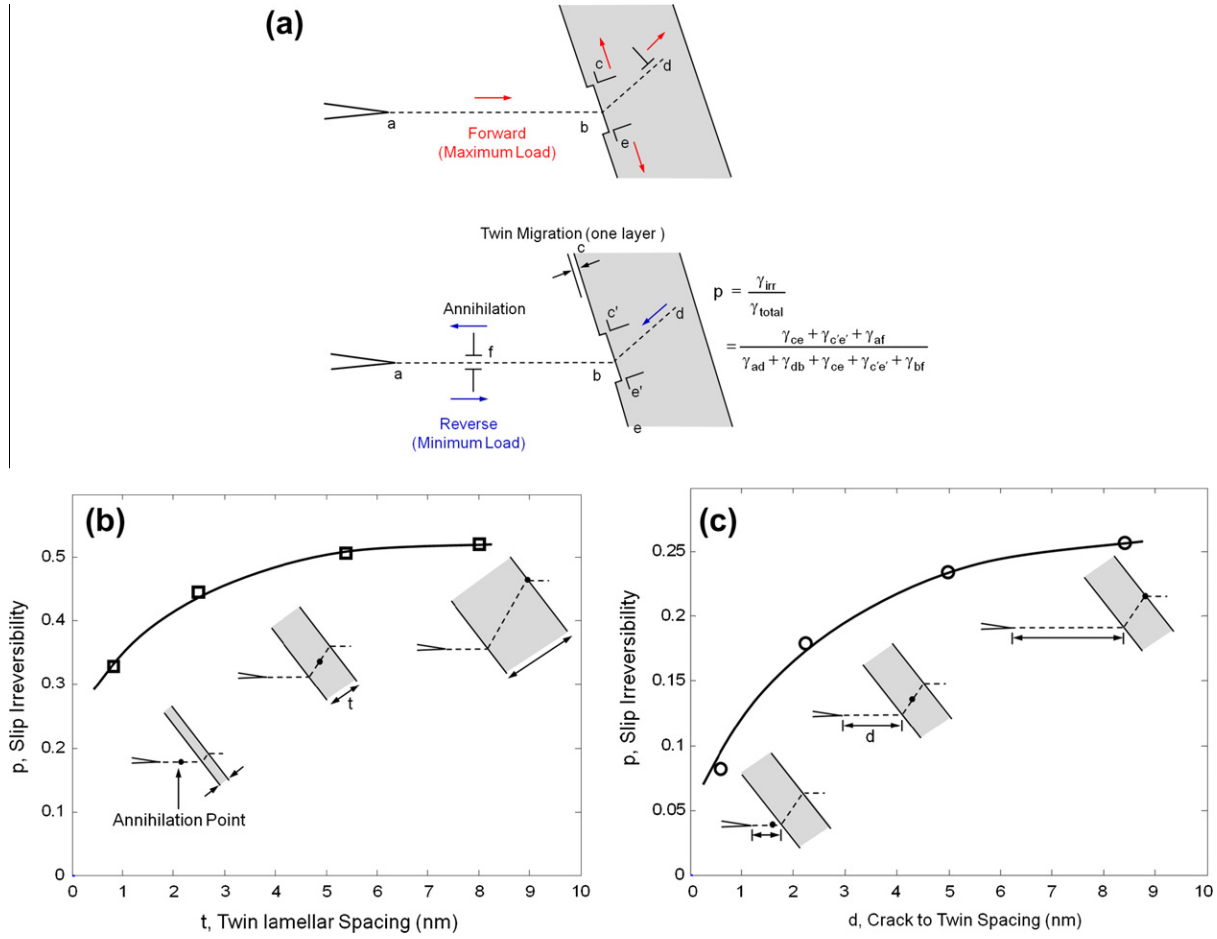

Fig. 5. (a) Schematic showing calculation of the slip irreversibility p. γ represents shear strains due to dislocation glide. (b) Slip irreversibility calculated from MD simulations as a function of crack tip to twin spacing t with constant $d = 80$ nm. (c) Slip irreversibility calculated from MD simulations as a function of the crack tip to twin spacing d with constant $t = 80$ nm.

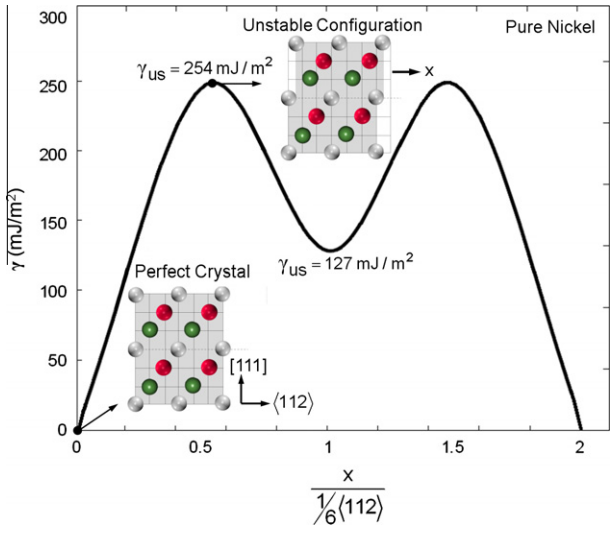

Fig. 6. Generalized stacking fault energy (GSFE) utilized in our study for pure nickel, calculated using the EAM potential developed by Foyles and Hoyt [43].

response of the system under investigation. The next section describes a detailed study of the CTB–dislocation interactions to clarify the reaction type.

3.1.1. Cyclical slip–twin interactions

MD simulations revealed the exact nature of the steady-state cyclical slip–twin reactions. During forward loading, after elastic straining, a perfect screw dislocation of Burgers vector $\frac{a}{2}[1\ \bar{1}\ 0]$ nucleates from the source on the most favorable slip system with the maximum resolved shear stress. Immediately after emission the perfect dislocation dissociates into two Shockley partials (leading and trailing) separated by a ribbon of stacking fault (Eq. (1)).

$$\underset{\text{Full}}{\frac{a}{2}[1\ \bar{1}\ 0]} \rightarrow \underset{\text{Leading}}{\frac{a}{6}[2\ \bar{1}\ 1]} + \underset{\text{Trailing}}{\frac{a}{6}[1\ \bar{2}\ \bar{1}]} + \text{Stacking Fault} \quad (1)$$

Under continued application of forward shear loading the extended dislocation (with a leading and a trailing Shockley partial) glides towards the CTB (Fig. 4a). Being obstructed by the CTB, the two partials recombine and generate new screw dislocations at the site of incidence (Fig. 4b). The new dislocations similarly dissociate into Shockley partials. One of the new dislocations is incorporated into the CTB as twinning partials, and another (extended) is transmitted inside the twin (Fig. 4c). Eq. (2) summarizes this reaction. Transmitted partials $\frac{a}{6}[\bar{2}\ \bar{1}\ 1]_T$ and $\frac{a}{6}[\bar{1}\ 1\ 2]_T$ become $\frac{a}{6}[2\ 1\ \bar{1}]_T$ and $\frac{a}{6}[1\ \bar{1}\ \bar{2}]_T$, respectively,

in the matrix frame. The total Burgers vector is then conserved on both sides of Eq. (2). Fig. 4d provides a double Thompson's tetrahedron depiction of the forward slip–twin reaction.

$$\underbrace{\underset{\text{Leading}}{\tfrac{a}{6}[2\bar{1}1]} + \underset{\text{Trailing}}{\tfrac{a}{6}[1\bar{2}\bar{1}]}}_{\text{Incident (Matrix)}} \rightarrow \underbrace{\underbrace{\underset{\text{Twininng}}{\tfrac{a}{6}[\bar{1}\bar{1}2]} + \underset{\text{Twinning}}{\tfrac{a}{6}[1\bar{2}1]}}_{\text{Incorporated (CTB)}} + \underbrace{\underset{\text{Trailing}}{\tfrac{a}{6}[\bar{2}\bar{1}1]_T} + \underset{\text{Leading}}{\tfrac{a}{6}[\bar{1}12]_T}}_{\text{Transmitted (Twin)}}}_{} \tag{2}$$

Until the end of the forward loading cycle the twinning partials on the CTB carry on gliding in opposite directions, gradually increasing their separation distance in order to minimize the elastic strain energy. Because of the gliding of these twinning partials the twin boundary migrates one atomic layer. The transmitted partials inside the twin continue to glide. As the load is reversed (unloading) the previously transmitted leading and trailing partials (inside the twin) now reverse their directions of motion (upon elastic relaxation). The returning extended dislocation interacts with the CTB and undergoes similar multiplication, thereby creating two new twinning partials on the CTB and two Shockley partials in the matrix. Eq. (3) describes the reverse reaction. The total Burgers vector (upon conversion of twin dislocations to the matrix frame) on both sides is conserved.

$$\underbrace{\underset{\text{Leading}}{\tfrac{a}{6}[\bar{2}\bar{1}1]_T} + \underset{\text{Trailing}}{\tfrac{a}{6}[\bar{1}12]_T}}_{\text{Returning (Twin)}} \rightarrow \underbrace{\underbrace{\underset{\text{Twinning}}{\tfrac{a}{6}[1\bar{2}1]} + \underset{\text{Twinning}}{\tfrac{a}{6}[2\bar{1}\bar{1}]}}_{\text{Incorporated (CTB)}} + \underbrace{\underset{\text{Leading}}{\tfrac{a}{6}[\bar{1}1\bar{2}]} + \underset{\text{Trailing}}{\tfrac{a}{6}[12\bar{1}]}}_{\text{Transmitted (Matrix)}}}_{} \tag{3}$$

With further unloading the twinning partials continue to glide in opposite directions, eventually causing twin migration by one atomic layer. The twin migration process may involve growth or shrinkage of the twin depending on the direction of motion of the participant twinning partials. The matrix Shockley partials continue gliding towards the source until a full dislocation (which also dissociates to become extended) of opposite sign nucleates from the source, meets with the returning one, and they annihilate each other. At the end of unloading another new negative dislocation (considering the original nucleated slip, at the beginning of forward loading, to be of positive type) nucleates and glides towards the twin, repeating the mechanism over subsequent cycles.

Table 1 summarizes the slip–twin reactions. Here b_s, b_e and b_r refer to the screw, edge component, and residual dislocation on the CTB, respectively. In summary, the reaction process involves transmission of unobstructed slip past the CTB (designated outgoing), and incorporation of slip with b_r in the CTB. The full dislocations are of pure screw type (which dissociate into partials) for both the incident and outgoing systems. For all the active slip systems the resolved shear stress τ_{RSS} under global applied stress τ is calculated using the formulation:

$$\tau_{RSS} = \sigma_{ij} m_i n_j \tag{4}$$

In Eq. (4) σ_{ij} is the remote stress tensor, m_i the slip plane normal vector, and n_i the vector representing the slip direction. For our case the applied σ_{ij} is reduced to τ_{13} (τ in Fig. 3). As can be seen in Table 1, the magnitudes of the ratio of τ_{RSS} to τ, defined as the Schmid factor (SF), for the active slip systems are fairly high. The maximum SF is operative on the CTB, which facilitates the incorporation of glissile twinning partials. The next largest SF acting on the outgoing slip system inside the twin assists in the transmission of slip past the CTB. The analyses, as summarized in Table 1 and Fig. 4, concern forward flow of slip past the CTB. However, the reverse reaction is modified only in the form of enhanced resistance (due to the presence of twinning partials in close vicinity) at the CTB. The reverse incidence of slip upon the CTB results in similar interaction products from dislocations at the reaction site. For more complex cases involving a multitude of incident dislocations (at larger t and/or d with a higher applied load) the interaction type remains fundamentally identical, undergoing simultaneous incorporation and transmission of slip. The subsequent sections address quantification of the slip irreversibility and the origin of the discrepancy of forward vs. reverse slip resistance at the CTB.

Table 1
Summary of cyclical steady-state slip–twin interaction.

Schmid factors (τ_{RSS}/τ)			Slip–twin interaction(s)	Incident slip (matrix)		Outgoing slip (twin)		Residual slip (CTB)
Incident	CTB	Outgoing		b_s	b_e	b_s	b_e	b_r
0.778	1.0	0.778	Transmission, incorporation	$\frac{a}{2}[1\,\bar{1}\,0]$	0	$\frac{a}{2}[1\,\bar{1}\,0]_T$	0	$\frac{a}{2}[0\,1\,\bar{1}]$

3.1.2. Cyclical slip irreversibilities

Fig. 5a shows a simple example of how irreversible dislocation glide during cyclical loading can be quantified, considering the case of a single incident dislocation (at smaller t or d). Steady-state cyclical slip–twin interaction involves the incidence of a dissociated full dislocation (screw) on the CTB. The reaction results in the simultaneous incorporation and transmission of extended dislocations. The final locations of these dislocations are at positions c and e (partials) and d (extended full dislocation, shown as full for simplicity) at the end of forward loading. The partials at c and e contribute to migration of the twin by one atomic layer. During reverse flow the extended dislocation at position d is transmitted back into the matrix, again leaving new partials at c′ and e′, which repulse the partials at c and e. The returning crack-bound extended dislocation is annihilated by another incoming dislocation of opposite sign (negative) at location f. We calculated the ratio p between the irreversible plastic shear strain γ_{irr} and the total plastic shear strain γ_{total} generated by dislocation glide over a cycle using Eq. (5). These γ values represent shear strains due to dislocation glide as they appear in Eq. (5). Even though Fig. 5a shows the cyclical process involving only one incident dislocation, on gradually increasing t and/or d a number of dislocations will contribute to the overall irreversible phenomena in an identical manner. The parameter p is then computed as a varying function of t and d. Fig. 5b and c demonstrates the results.

$$p = \frac{\gamma_{irr}}{\gamma_{total}} = \frac{\gamma_{ce} + \gamma_{c'e'} + \gamma_{af}}{\gamma_{ad} + \gamma_{db} + \gamma_{ce} + \gamma_{c'e'} + \gamma_{bf}} \tag{5}$$

The trend for cyclical crack tip slip irreversibilities p, as calculated in Fig. 5b and c, tends to become independent of t and d at sufficiently large magnitudes. At lower values of t and d a relatively small number of dislocations are emitted from the source and traverse the entire thickness of the twin. Consequently, a shorter spacing between the source and the twin as well as thinner twins will expedite the return of source-bound positive slip, and at the same time preclude gliding of negative slip sufficiently farther away from the source. Thus the annihilation process (location f in Fig. 5a) occurs in very close proximity to the source (as in the insets in Fig. 5b and c). As a result, the magnitude of p is low in the small t and/or d regime, as calculated with Eq. (5). However, an increase in t or d necessitates a larger applied load in order for slip to occur and traverse the twin. This results in a gradually greater number of dislocation emissions. The involvement of multitudes of dislocations leads to an increase in the pile-up stress during both forward and reverse flow. This results in even greater blockage of returning positive dislocations, thereby permitting unobstructed negative slip to travel further away from the source. As a result, the annihilation process occurs at a greater distance from the source (as indicated in the insets). Due to the involvement of large-scale slip activity for even higher t or d the annihilation point eventually settles at a stable unvarying position, corresponding to the plateau region in Fig. 5b and c.

The underlying origin of glide irreversibilities as influenced by CTBs can be traced back to the discrepancies in the energy pathways for slip for forward and reverse transmission across CTBs. Such a phenomenon modifies the resistance of slip penetrating the CTBs under cyclical conditions, as further discussed below.

3.1.3. Energy barrier and ideal glide strength

The potential energy variation–displacement relationship of a pair of partial dislocations (an extended full dislocation separated by a stacking fault) in an otherwise perfect fcc crystal is described by the GSFE, as in Fig. 6. During glissile slip motion sliding of atomic planes occurs by overcoming the unstable fault energy γ_{us} (inset in Fig. 6). The unmodified GSFE curve points to the resistance of dislocation glide scaling with γ_{us}, as imposed by the crystal. A Shockley partial dislocation glides on the (1 1 1) plane with the Burgers vector along the ⟨1 1 2⟩ direction. The modified GSFE takes the form of an increase in γ_{us} due to the presence of the CTB (or any other local stress sources), as shown in Fig. 7a. In order to compare the relative resistance encountered during forward and reverse flow the modified γ_{us} in the vicinity of a CTB is calculated (Fig. 7c).

With a view to estimating the resistance stress provided by a CTB to the approaching slip for back and forth transmission we calculated the modified GSFE in the vicinity of the CTB using a dynamic approach. Considering the dynamic nature of dislocation glide over time, computing the variation in the potential energy difference in some preselected atoms allows quantification of the modified GSFE (discussed in detail in Appendix A). The γ_{us} values derived from these modified energy curves are plotted as a function of distance normal to the CTB in Fig. 7c. In Fig. 7b the dislocation at A is approaching the CTB but is still unaffected by the stresses resulting from the matrix–twin interfacial atomic mismatch. Thus γ_{us} at A denotes the energy barrier that a dislocation has to overcome when it is gliding freely inside the crystal. The magnitude of γ_{us} at A matches the peak in Fig. 6, which represents the energy barrier to unobstructed gliding, amounting to 254 mJ m^{-2}. The local stress generated due to atomic mismatch at and around the CTB elevates γ_{us} once the approaching dislocation is in closer proximity. The maximum energy barrier that the incident dislocation needs to overcome is achieved when the slip interacts with the CTB, an intermediate step in formation of the final reaction products (Fig. 7b and c point B). The elevated energy at point B corresponds to a γ_{us} value as high as 340 mJ m^{-2}. Therefore the energy path A → B → C (red curve) describes the variation in γ_{us} for transmitted dislocations during forward flow. In the course of reverse flow the returning dislocation encounters an even greater energy barrier due to the presence of the dissociated twinning

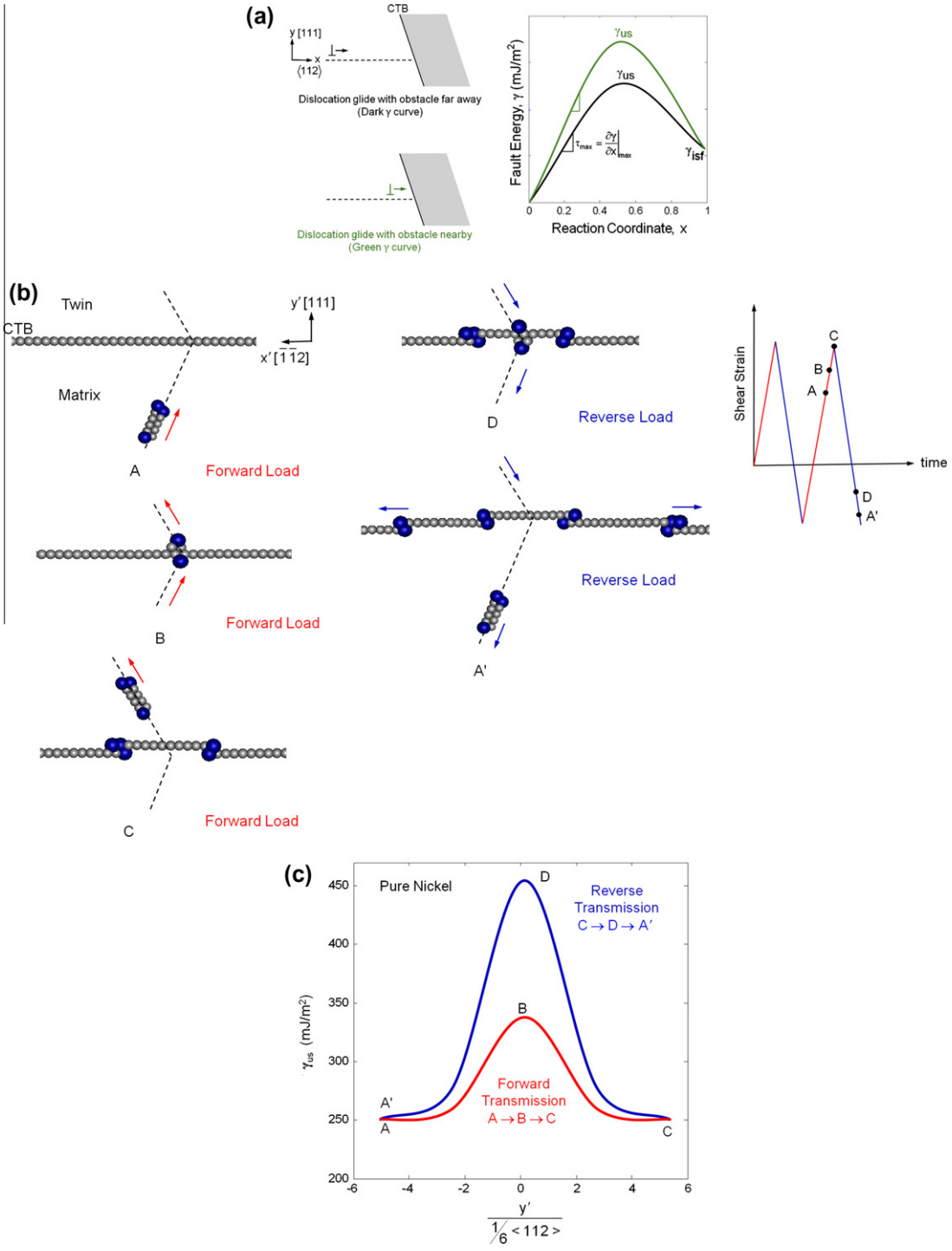

Fig. 7. (a) Schematic demonstrating the expected increase in energy barrier (γ_{us}) due to the presence of a local stress source. The dark line depicts the planar fault energy for dislocation glide through a perfect crystal, while the green line represents the enhanced energy encountered in the presence of a CTB. The maximum slope of the (un)modified GSFE equals the ideal shear stress of the crystal τ_{max}. Ezaz et al. [31] extensively explored the contribution of local stresses to the fault energetics of slip–twin interactions. (b) As a pair of Shockley partials approaches the CTB the energy barrier (γ_{us}) is elevated in the neighborhood of the twin–matrix interface. γ_{us} is maximum at the CTB (position B). At C the γ_{us} is the same as at A. Upon interaction with a CTB a pair of Shockley partials is left on the CTB, while another pair transmits into the twin. As the transmitted pair glides away from the interface γ_{us} decreases to the level of a perfect lattice barrier. During the reverse transmission upon flipping of loading the returning dislocation encounters enhanced γ_{us} due to the presence of the Shockley partials on the CTB (at point D). As the returning extended dislocation is transmitted back into the matrix it undergoes a similar multiplication, leaving another pair of twinning partials on the CTB. Schematic of load cycles in MD simulations (strain control) showing where A, B, C, D and A′ occur. (c) Change in unstable energy γ_{us} as a pair of partial dislocations approach a CTB during forward/reverse loading in the MD fatigue cycle. Path A → B → C provides an energy barrier against forward transmission (red curve), and C → D → A′ against reverse transmission. The energy at D is greater than at B because of the presence of dissociated Shockley partials on the CTB during reverse loading. (For interpretation of the references to color in this figure legend, the reader is referred to the web version of this article.)

partials on the CTB. Therefore the reverse energy barrier follows the path C → D → A′ (blue curve). The γ_{us} maximum reaches a magnitude of 452 mJ m^{-2} at point D. The elevation of the reverse transmission energy barrier compared with the forward barrier can be attributed to the increase in local stress around the CTB due to the residual twinning partials. The GSFE for slip glide, as modified in the above mentioned manner, facilitates calculation of the ideal shear strength of the crystal τ_{max}. τ_{max} is a function of γ_{us}, and is calculated from the maximum slope of the modified or unmodified GSFE curve (Eq. (6)). Applying corrections for thermal activation and strain rate to the plastic flow the ideal critical glide strength τ_o at room temperature and a typical experimental strain rate can be calculated. Eq. (7) implies that τ_o is also a function of strain rate ($\dot{\varepsilon}$), temperature (T), and activation volume (V^*). The procedure for obtaining τ_o is detailed in Appendix B.

$$\tau_{max} = \tau_{max}(\gamma_{us}) = \left.\frac{\partial \gamma}{\partial x}\right|_{max} \tag{6}$$

$$\tau_o = \tau_o(\tau_{max}, \dot{\varepsilon}, T, V^*) \tag{7}$$

Below we investigate continuum slip emissions from a fatigue crack whose glide paths become irreversible upon cyclical loading. Atomistically computed τ_o values are then utilized to characterize the continuum level dislocation glide, and subsequent fracture mechanics simulations.

3.2. Continuum dislocation simulations

We modeled a pre-existing mode III fatigue crack in the presence of a nanotwin. The crack emits a series of screw dislocations. These dislocations intersect the twin and, eventually, their cyclical glide paths become irreversible via annihilation. The slip glide resistance (due to lattice friction and penetrating twins) influences the equilibrium positions and the total glide path irreversibility. Cracks advance by accumulating plastic displacement at the tip, originating from the irreversibility of cyclical slip. For a given crack length (a), twin thickness (t) and twin position from the crack tip (d) and stress intensity levels (ΔK_{III}) we can predict the corresponding values of da/dN. da/dN is expressed as a function of the equilibrium positions of discrete dislocations at a certain ΔK_{III}.

3.2.1. Fracture mechanics calculations

In the continuum model we selected a mode III fatigue crack and the associated emission of pure screw dislocations (Fig. 8). The MD derived glide strengths for a screw dislocation were utilized. The continuum dislocations can overcome the glide resistances under the applied external load, and eventually assume equilibrium positions. At the equilibrium position a dislocation emitted from a crack tip experiences three forces: (1) resolved applied shear stress $\tau_{Applied}$; (2) image stress τ_{Image}; (3) pile-up stress $\tau_{Pile\text{-}up}$. With the nucleation of new dislocations the local stress at the crack tip decreases due to enhanced image and pile-up stress. In order to compensate for this decrease

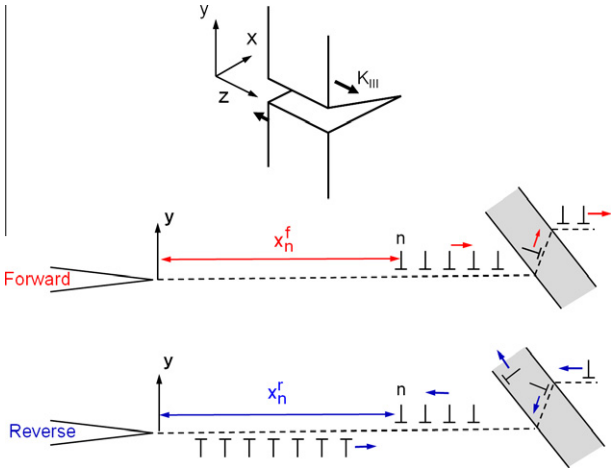

Fig. 8. The set-up for dislocation dynamics simulations. A mode III crack emits a series of screw dislocations that glide away to interact with a nanotwin of finite lamellar width placed at a finite distance. Positive dislocations assume equilibrium positions x_n^f and x_n^r during forward and reverse loading, respectively. Negative dislocations nucleate during the reverse half cycle, and eventually annihilate returning positive dislocations.

the applied load has to be increased to facilitate further nucleation. Thus Eq. (8) summarizes the net shear stress τ_n acting on the nth dislocation.

$$\tau_n = \tau_{Applied} - \tau_{Image} - \tau_{Pile\text{-}up} \tag{8}$$

τ_n is formulated in Eq. (9).

$$\tau_n = \underbrace{\frac{K_{III}}{\sqrt{2\pi x_n}}}_{\text{Applied}} - \underbrace{\frac{\mu b}{4\pi x_n}}_{\text{Image}} - \underbrace{\frac{\mu b}{2\pi x_n}\sum_{i\neq n}\sqrt{\left(\frac{x_i}{x_n}\right)}\frac{1}{x_i - x_n}}_{\text{Pile-up}} \tag{9}$$

Eq. (9) gives τ_n as a function of K_{III}, the applied global stress intensity factor for mode III loading, μ, the shear modulus, b, the Burgers vector, and x_n, the location of the nth dislocation along its glide path from the source (crack tip). τ_n ought to be of sufficiently large magnitude in order for slip to overcome the unstable energy barrier (γ_{us}). Therefore with increasing global applied loading τ_n needs to surpass and/or equal τ_o to initiate glide. Thus Eq. (10) provides the conditions for gliding, which is further rearranged to formulate Eq. (11).

$$\tau_n \geqslant \tau_o \tag{10}$$

$$\frac{K_{III}}{\sqrt{2\pi x_n}} - \frac{\mu b}{4\pi x_n} - \frac{\mu b}{2\pi x_n}\sum_{i\neq n}\sqrt{\left(\frac{x_i}{x_n}\right)}\frac{1}{x_i - x_n} - \tau_o = 0 \tag{11}$$

Eq. (11) provides the equilibrium conditions for dislocations. The final equilibrium positions (x_i) of all dislocations during both forward and reverse loading (at maximum K_{III}) were solved from Eq. (11). These x_i values were utilized as the input for a FCG rate formulation (discussed later in Eq. (15)).

In order to clarify the procedure for the mechanics-based simulations let us consider a simple case consisting of a very low applied ΔK_{III} such that cyclical crack tip plasticity involves only one discrete dislocation (designated 1 in

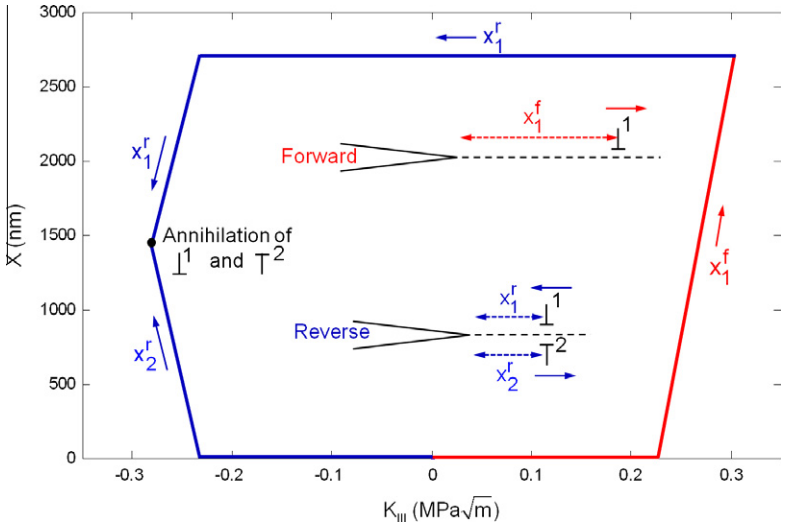

Fig. 9. A single dislocation demonstrating the slip trajectory during da/dN calculations. A mode III crack emits a screw dislocation (designated 1) during forward loading which assumes an equilibrium position at maximum forward load (trajectory shown in red). During reverse loading (blue trajectory), after elastic relaxation the dislocation starts to return, and is annihilated by a newly nucleated dislocation of opposite sign (designated 2). (For interpretation of the references to color in this figure legend, the reader is referred to the web version of this article.)

Fig. 9) with no obstacle (twin) in the glide path. At a certain time point in the loading cycle the forward (x_1^f) and reverse (x_1^r) equilibrium positions of the disloction are solved by setting the lattice friction stress equal to the applied resolved shear stress. In the forward half-cycle as the applied load is increased the dislocation continues to glide away until the maximum K_{III} is reached. Fig. 9 demonstrates the trajectory for the case of a single dislocation during forward/reverse loading. In forward loading a dislocation nucleates at a critical K_{III} value and then glides away to assume its final position (red curve). During reverse loading the dislocation does not immediately start to return towards the crack tip because of elastic strain recovery. As the shear stress in the reverse direction exceeds the lattice friction resistance it starts to glide towards the crack tip and eventually is annihilated by a newly nucleated negative dislocation. Continued reverse loading triggers the nucleation of another negative dislocation which repeats the mechanism over another cycle. This simplistic demonstration of the irreversiblity of a discrete dislocation glide path over a fatigue cycle elucidates the fundamental procedure of the continuum-based simulations.

The introduction of nanoscale twins on the glide path of slip modifies the total irreversibility as well as slip obstruction by the crack. Eq. (12) provides an evaluation of the slip irreversibility parameter p (previously defined as the ration between γ_{irr} and γ_{total}) as a function of the dislocation positions at equilibrium during forward and reverse flow (denoted by the superscripts f and r, respectively).

$$p = \frac{\gamma_{irr}}{\gamma_{total}} = \sum_{i=1}^{n} \frac{x_i^r}{2x_i^f - x_i^r} \tag{12}$$

Fig. 10 shows the evolution of p as evaluated with the specified values of t at constant d, with a change in the applied stress intensity factor range. p increases non-

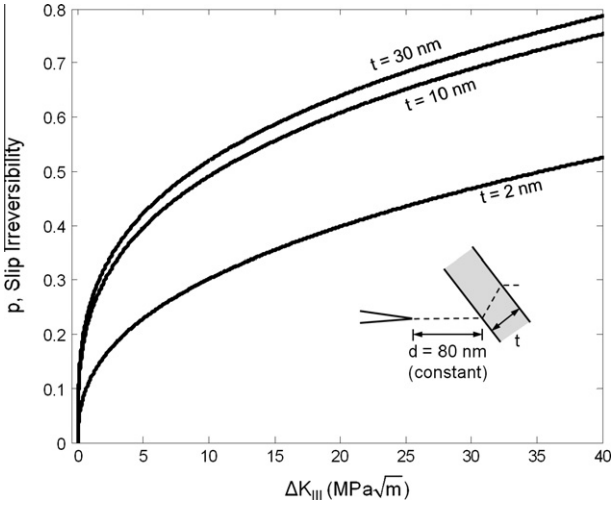

Fig. 10. Irreversibility of crack tip emitted dislocation activities for three cases of finite nanotwin lamellar spacings.

linearly (square root trend) with ΔK_{III}, and eventually achieves a plateau. The computed tendency of p highlights the functional dependence of irreversible glide phenomena, and hence the crack tip plasticity, on the variation in twin thickness t on the nanoscale. This is consistent with the MD calculations elucidated earlier in Fig. 5b and c. In response to changes in the twin lamellar width the equilibrium positions of dislocations change accordingly. This would lead to different degrees of irreversibility in the overall dislocation glide paths, as implied through Eq. (12). These results points to a change in FCG rate as a function of t or d. In order to further explore the t and/or d dependence of FCG a comparison of da/dN under such conditions was evaluated.

3.2.2. FCG simulations

A cyclical crack accumulates plastic displacement on an incremental basis. If there are n dislocations emitted from the crack tip the plastic displacement at the tip caused by each emission contributes to the overall crack extension. Based on the formalisms introduced earlier the rate of crack tip advancement per cycle can be formulated as:

$$\frac{da}{dN} = \int_0^{x^f_{max}} du \tag{13}$$

$$\frac{da}{dN} = \frac{x^f_{max}}{2\mu}\sum_{i=1}^{n}(\tau^f_n - \Delta\tau_n) \tag{14}$$

In Eq. (13) x^f_{max} is the maximum distance away from the crack during forward loading traveled by the farthest dislocation, u is the crack tip displacement as a function of x_i and μ is the shear modulus in the slip direction, τ^f_n is the shear stress at the end of the forward half-cycle (a function of x^f_i), and $\Delta\tau_n$ is associated with the distance (x_i) traveled by the returning crack bound dislocations (a function of $x^f_i - x^r_i$). Combination of Eqs. (9) and (14) leads to the da/dN formulation given in Eq. (15). In this formalism da/dN is essentially a function of the equilibrium dislocation positions. The solutions for these slip locations (x_i) at the maximum K_{III}, as obtained from the equilibrium condition (Eq. (11)) during forward/reverse flow, provide input to the da/dN evaluation. Calculation of da/dN in this manner inherently incorporates the atomistically computed ideal glide stress as well as the twin penetration strength.

$$\begin{aligned}\frac{da}{dN} = {} & \frac{x^f_{max}\Delta K_{III}}{2\mu\sqrt{2\pi}}\sum_{i=1}^{n}\left(\frac{1}{\sqrt{x^f_i}} - \frac{1}{\sqrt{x^f_i - x^r_i}}\right) \\ & - \frac{x^f_{max} b}{8\pi}\sum_{i=1}^{n}\left(\frac{1}{x^f_i} - \frac{1}{x^f_i - x^r_i}\right) \\ & - \frac{x^f_{max} b}{4\pi}\sum_{i=1}^{n}\sum_{j\neq i}\left(\sqrt{\left(\frac{x^f_j}{x^f_i}\right)}\frac{1}{x^f_j - x^f_i}\right. \\ & \left. - \sqrt{\left(\frac{x^f_j - x^r_j}{x^f_i - x^r_i}\right)}\frac{1}{(x^f_j - x^r_j) - (x^f_i - x^r_i)}\right)\end{aligned} \tag{15}$$

We employed the da/dN formulations from Eq. (15) to quantitatively investigate the sensitivity of the slip blocking strength of nanotwins against FCG. Fig. 11 demonstrates that for a twin placed at a large distance d from the crack tip (of the order of 1000× the Burgers vector) FCG becomes totally independent of the resistance of the interface to the interacting slip. Thus such a calculation provides information regarding the critical zone of influence of the CTB. As shown in Fig. 11, the critical interface influence size resides in the plateaux regions for which da/dN is independent of the slip-blocking strength at small d values. The CTB influence zone ranges across a few Burgers vector values, consistent with the MD findings (Fig. 7c). Determination of the neutral CTB influence size assists in the calculation of FCG as a function of t and d.

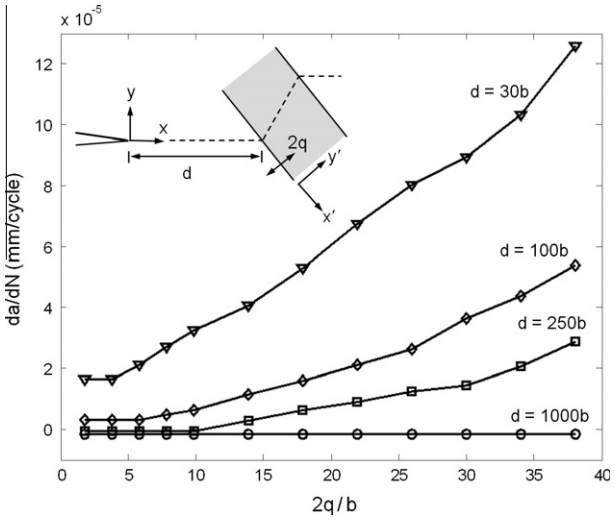

Fig. 11. Determination of the critical matrix–twin interface zone size ($2q$).

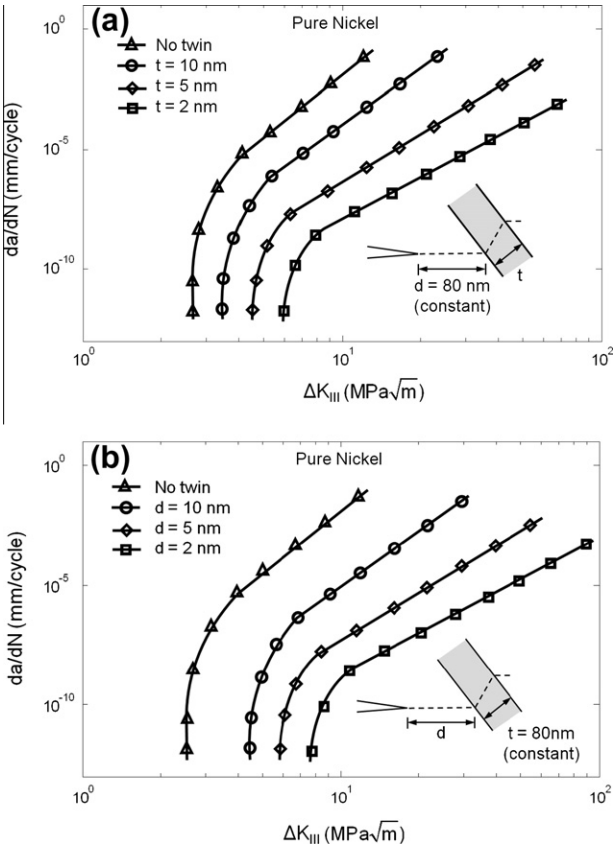

Fig. 12. (b) da/dN vs. ΔK_{III} plots demonstrating the influence of (a) twin width and (b) crack to twin distance on FCG and the threshold properties.

Fig. 12a and b shows how the FCG metrics change with variations in t and d, as predicted earlier in the evaluation of cyclical slip irreversibilities in Fig. 10. These plots of da/dN vs. the applied ΔK_{III} reveal a t and d dependence of the rate of FCG as well as the threshold behavior. For smaller t and/or d FCG is significantly influenced by the nanotwin

dimensions. Thinner twins as well as twins placed very close to the crack tip lead to enhanced FCG metrics.

4. Discussion

4.1. Cyclical slip–twin interactions and irreversibilities

Earlier works have pointed out the role of the local stress state and the type of dislocation (screw, edge or mixed) in dictating the nature of dislocation–CTB interactions [31,45]. In the present work we have examined the cyclical slip–twin interaction mechanism for fatigue crack tip-nucleated dislocations. Table 1 summarizes the observed dislocation–CTB reactions during forward flow. Our case consists of pure screw incident dislocations that glide and intersect with the CTB. In the literature the incidence of a screw dislocation upon a coherent twin reportedly activates one of two mechanisms [7,46]: (i) incorporation (absorption) of the incident dislocation followed by dissociation into Shockley partials on the CTB; (ii) direct transmission of the incident dislocation through the twin. We observed that the incident dislocation causes nucleation of dislocations at the reaction site, as described in Fig. 4c. As listed in Table 1, the SFs on the CTB and outgoing system are 1.0 and 0.778, respectively, which are sufficiently high to facilitate the reaction observed. This reaction consists of simultaneous incorporation and transmission of glissile dislocations on and across the CTB, as shown in Fig. 4c. As clarified in the recent literature, blocking of slip by CTBs (incorporation) promotes to a considerable extent macroscopic ductility, by allowing dislocation glide along the interface, unlike incoherent GBs [7]. This special feature of CTBs, along with permitting transmission, results in an enhancement of the macroscopic mechanical properties. Sangid et al. [21] ascribed the balance of macroscopic strength and ductility of nanotwinned materials to the superior FCG metrics. As per our observations, the types of slip–twin interactions which promote both strength and ductility on the micro-scale are operative during to and fro glissile motions of slip across nanotwins.

Farkas et al. [36], Nishimura and Miyazaki [37] and Potirniche et al. [38] studied the mechanism of fatigue crack advancement through the nucleation and coalescence of nanovoids formed due to crack tip slip activity by MD. While these simulation studies addressed the FCG mechanism experimentally observed in especially the smaller sized (<30 nm) nanograined materials [47,48], cyclical irreversible slip activity as the underlying driving force of crack propagation was not particularly explored from a mechanistic perspective. We observed that the obstruction of slip and accumulation of crack tip displacements, as dictated by glide path irreversibility, were both influenced by the presence of CTBs. The calculation of glide path irreversibilities further illuminates an understanding of the mechanism of FCG in the presence of coherent twins, as presented in Fig. 5b and c.

The quantified cyclical slip irreversibility p tends to become independent of t and/or d at sufficiently large magnitudes of these dimensions, as shown in Fig. 5b and c. We observed a decrease in p to a value indicating almost completely reversible slip for the case of a crack tip (source) located in close proximity to nanotwins, and also for twins with diminishing lamellar spacings. This trend could be attributed to the limited availability of slip gliding space for the case of smaller t or d, aided by the expedited return of dislocations upon reversal of loading. The reduced space allows a smaller degree of glissile motion by newly nucleated negative dislocations towards the CTB along the same slip system as positive slip during forward flow. This permits the returning crack-bound positive slip to undergo annihilation with negative dislocations in the close neighborhood of the source (crack tip).

The observed trends of quantified irreversible dislocation activity, as in Fig. 5, possess important implications regarding the mechanism of crack advancement in the presence of nano-obstacles. The fundamental mechanism of fatigue crack advancement is governed by the cyclical irreversibility of crack-nucleated dislocations during cycling. The nano-obstacles render the dislocation glide path irreversible by holding back the returning dislocations. Hence, if the obstacle (a coherent nanotwin in our case) promotes lowering of the cyclical slip irreversibility plastic displacement at the crack would be suppressed accordingly. Therefore, FCG is expected to be at a reduced rate, along with similar changes in the characteristic microstructural dimensions (t and d) at lower magnitudes. The underlying reason for cyclical slip irreversibility can be traced back to energy barriers to slip transmission on the atomic length scale at matrix–twin interfaces during the forward and reverse fatigue half-cycles. The discrepancies in forward and reverse transmission energy trigger the irreversibility of dislocation gliding, resulting in the accumulation of local plastic displacement at the crack tip.

Calculation of the energy barriers (γ_{us}) in the vicinity of the CTB for the forward and reverse fatigue half-cycles explains the discrepancies between the forward and reverse transmission strengths, as illustrated in Fig. 7c. The energy pathways for the forward (red curve along $A \rightarrow B \rightarrow C$) and reverse (blue curve along $C \rightarrow D \rightarrow A'$) transmission of slip across the CTB are markedly different. This enhanced energy barrier necessitates a greater resolved shear stress acting on the returning dislocations to force them back into the matrix, as they approach the CTB from within the twin. This, in turn, requires application of a higher global loading for such a reverse transmission of slip. As a result, the crack-bound dislocations are delayed at the CTB during the reverse half-cycle. This delay allows negative dislocations to nucleate from the crack and glide towards the CTB along the same slip system, meeting the reversing positive slip.

As observed, the principal mechanism of slip irreversibility over fatigue cycles is the impedance to gliding of returning dislocations by residual dislocations on the

CTB. The enhanced energy barrier during reverse flow owing to this residual slip on the CTB would pose a greater degree of obstruction to reversing dislocations. The present work quantifies the degree of glissile irreversibility as related to the characteristic microstructure dimensions, as well as captures the governing physics in terms of the underlying energetics. Even though the present study is limited to discussions of cases concerning only screw dislocations, similar physics are expected for edge and mixed dislocations. Pure edge or mixed dislocations leave residual dislocations on the CTB upon interacting with coherent twins, as examined earlier in the literature [6,7,31,49]. Despite the varied nature of slip–twin reactions from case to case, the enhanced resistance encountered by reversing slip and their subsequent annihilation by dislocations of opposite sign would occur in a similar generalized pattern for mixed or pure edge cases. Hence the overall irreversible glide path pattern would essentially be identical with similar trends in FCG characteristics.

4.2. Role of microstructural dimensions on FCG

In the fracture mechanics simulations of a mode III fatigue crack emitting screw dislocations the cyclical slip irreversibility p is again evaluated as a function of the applied stress intensity factor. In Fig. 10 the functional dependence of p on ΔK_{III} shows a square root trend. This could be attributed to the involvement of multitudes of dislocations that glide away to interact with the nanoscale obstacle (twin) at larger K_{III}. The forces barring gliding of dislocations away from the source (originating from increasing pile-up and image stress) restrict dislocation movement to a greater extent at larger K_{III}. Mughrabi [50] summarized the estimated cyclical slip irreversibilities, which were experimentally found to be almost negligible at low loading amplitudes (leading to a long fatigue life), and close to unity at larger loading amplitudes (resulting in a short fatigue life). For diminishing twin lamellae spacings the irreversibility also decreased, as depicted in Fig. 10. The mechanism lies in the lowered capability of thinner twins to hold back dislocations at larger applied K_{III}, resulting in a low slip irreversibility.

Another important question regarding the transmission stress required for dislocations to penetrate these nanoscale obstacles is illustrated in Fig. 11. From the MD simulations we can estimate the critical twin–matrix interface zone size as normalized by the Burgers vector within which the CTB stress field would effectively elevate the energy barrier to transmission (Fig. 7c). The effective range of the interface influence zone size is in the range of a few multiples of the Burgers vector. To determine the role of the penetration strength of the nanotwins we looked at the evolution of da/dN at constant K_{III} with a varying degree of CTB influence zone (i.e. transmission strength of the twins). The results, shown in Fig. 11, indicate a neutral plateau in da/dN at low $2q/b$ for varying twin to crack spacings, where q is the distance from the twin–matrix interface. For twins located far enough from the crack the rate of FCG is independent of the influence of dislocation transmission stress. We chose a value of $2q$ in this neutral plateau for subsequent da/dN vs. ΔK_{III} simulations in order to compare the role of t and/or d on the FCG properties.

The continuum simulation framework involving discrete dislocations provides quantitative evidence of a role of the microstructural dimensions t and d in FCG. Fig. 12a and b demonstrates how the change in any one of these microstructural characteristic lengths (with the other being kept constant) affects da/dN. As can be seen, both the Paris and threshold regimes are influenced by such a variation in t or d. For a decrease in either the width of the nanotwin lamella or the twin to crack tip spacing da/dN also decreases. Crack advancement in the threshold regime is minuscule by nature, and is characterized by cycle by cycle discrete plasticity. Our approach of modeling the crack tip plasticity accounts for individual dislocation contributions, thereby faithfully capturing the incremental crack growth for both massive and minute slip activities.

The results have important implications in understanding mode II (shear mode) fatigue crack growth, as well where edge dislocations are emitted from the crack tip. Although at the continuum level the description of edge and screw dislocations are similar, as noted by Pippan, the reactions at the boundaries and residual dislocations will differ, necessitating a complete analysis with corresponding MD simulations. This may explain the fundamental differences between different threshold levels observed in the literature for mixed mode loading cases.

In summary, the critical microstructural characteristic lengths (t and d) associated with these obstacles play a pronounced role in FCG simulations. The correlation of FCG metrics with the change in these characteristic microstructural dimensions is governed by variations in the irreversibility and blockage of slip emitted from the crack tip interacting with an annealing nanotwin in the vicinity. FCG progresses via a combination of these two phenomena as influenced by nanotwins. If the CTB permits a reduced degree of cyclical slip irreversibility the cyclical crack extension will act likewise. Therefore, FCG is expected to occur at varying rates corresponding to the changes in these characteristic microstructural dimensions (t and d). The insight obtained from such observations further clarifies the mechanism of cycle by cycle crack propagation. Slip irreversibility increases non-linearly as these characteristic lengths become greater, eventually reaching saturated levels. Similar trends in da/dN with respect to changes in spacing of the twin to the crack tip or the twin lamella thickness are observed in the continuum FCG simulations. Fig. 12a and b summarizes the variations in da/dN with these changes in the microstructural characteristic nanodimensions, thereby mapping the crack growth regimes. The trends in FCG in these calculations are consistent with earlier experimental findings in the literature as reported by Sangid et al. [21] and Singh et al. [5].

5. Conclusions

Utilizing MD and fracture mechanics simulations of discrete dislocation formulations we have studied the mechanism of FCG at the appropriate length scale by quantifying cyclical slip irreversibilities. Our goal was to isolate the role of nanotwins in the mechanism of FCG, as brought to our attention by recent experimental findings. The major contributions of this work can be summarized as follows.

1. The analysis presented in this study underscores the role of twin spacing and twin lamellar width on FCG. We note that the influence of these nanodimensions becomes more prominent when the twin spacing and twin width are typically less than 20 nm. The increase in FCG resistance is governed by the modified cyclical slip irreversibility and dislocation annihilation behavior upon slip–twin interaction. The FCG metrics, such as da/dN and the threshold stress intensity range, are increased to a substantial extent on refinement of the nanotwin spacing and thickness. However, as these characteristic dimensions increase their role in FCG becomes less.
2. The investigation unfolded enhanced energy barriers for slip to glide across nanoscale CTBs owing to the presence of residual dislocations during reverse flow under cyclical conditions. Quantification of the mismatch in energy barriers to to and fro glide across twins provides a physical explanation for the irreversible glissile motion of slip. Such an insight extends our mechanistic understanding of previously observed experimental findings on FCG as influenced by nanoscale twins.
3. Considerable attention has been devoted to ensuring convergence of the unstable energy values when choosing fault dimensions of the order of the dislocation core. The sensitivity of the selected area of atoms to the unstable energy values was determined for dislocation advance in the matrix and near CTBs. In addition, the friction stress levels were scaled to account for the strain rate and temperature effects. As a result, the differential in friction stress upon forward and reverse loading was shown to play the most significant role in FCG.

Acknowledgements

Support for this work was provided primarily by Honeywell Aerospace Corporation. We acknowledge the use of the parallel computing resource, the Taub cluster, at the University of Illinois.

Appendix A

Since dislocation glide occurs via motion of the core through consecutive tearing and forming of atomic bonds around the core the sequential rows of atoms on the slip plane ahead of the oncoming dislocation alternately come within the influence of the mobile core. Therefore, by calculating the variation between the enhanced potential energy (E) of such atoms and the bulk perfect lattice energy (E_{perfect}) one would be able to compute the γ surface (using Eq. (A1) after Vitek et al. [44]). We devised a novel technique of calculating the fault energies during dynamic slip motion.

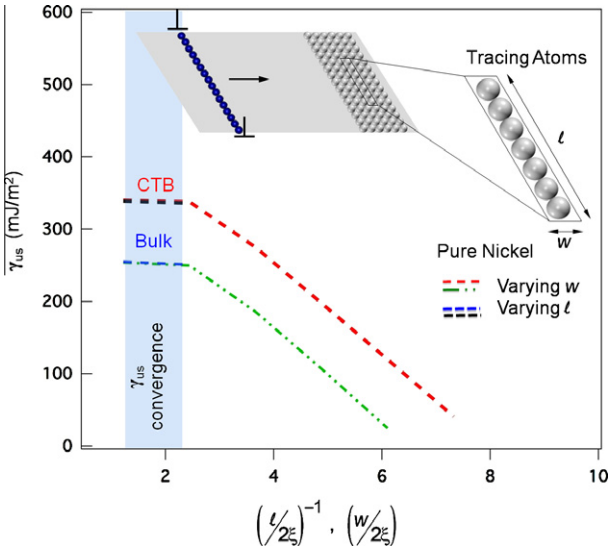

Fig. A1. The sensitivity of the calculation of γ_{us} (bulk and CTB) on the length scale of the chosen tracing atoms. The desired ranges of l and w (normalized by the theoretical core width of a screw dislocation 2ξ [51]) for tracing the potential energy variation due to the oncoming dislocation is highlighted. γ_{us} (bulk and/or CTB) converges with increasing l and decreasing w.

$$\gamma = \frac{E - E_{\text{perfect}}}{A} \tag{A1}$$

Ahead of an oncoming dislocation a group of atoms, designated tracing atoms (with an area on the slip plane $A = wl$ in Fig. A1), were carefully selected, where l and w are the distances parallel and normal to the dislocation line, respectively. The curves in Fig. A1 substantiate the length scale independence of modified/unmodified γ_{us} on the range of the selected tracing area dimensions (normalized by the theoretical core width of a screw dislocation, $2\xi \approx d$ where d is the interplanar distance ($d \approx 2.03$ Å for nickel) between (1 1 1) slip planes [51]).

A large w value spreading beyond the influence of the core distortion encompasses lower energy bulk atoms in the calculation, therefore the normalized values are sufficiently small for convergence, as shown in Fig. A1. The value of l was also selected to ensure convergence, as again shown in Fig. A1. The energy of the tracing atoms was confirmed to have a γ_{us} value consistent with density functional theory. For the case of an extended dislocation, as the leading Shockley partial approaches the tracing atoms the value of γ starts to increase, and achieves a maximum value γ_{us} when the leading partial passes it. The departing leading partial leaves a stacking fault behind in its wake. At this point γ assumes the value γ_{isf}. As the trailing partial translates the value of γ in the tracing area again starts to

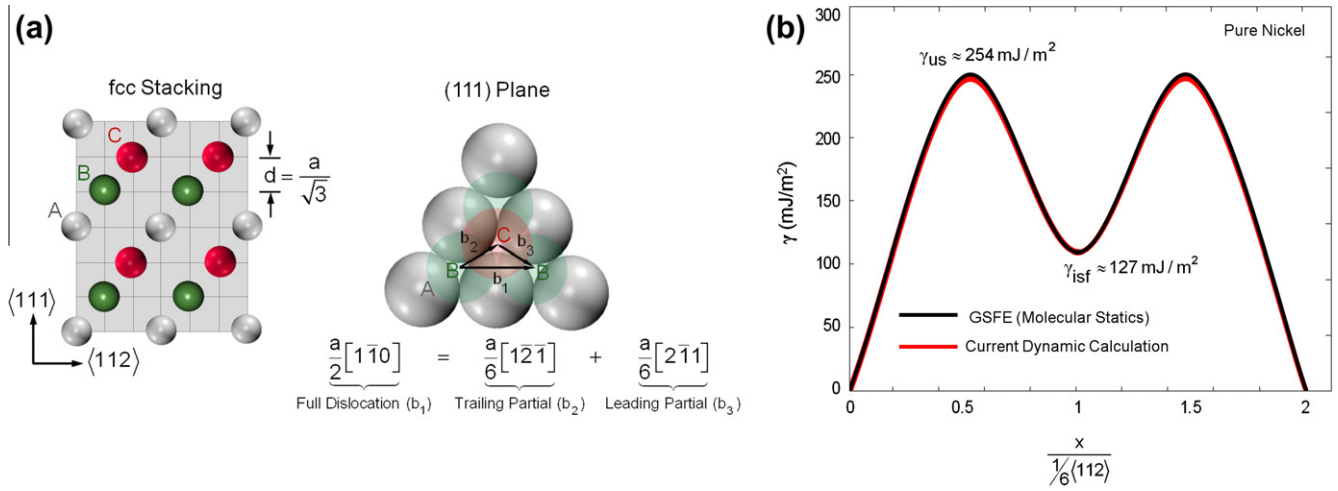

Fig. A2. (a) Schematic demonstrating the atomic configuration of the fcc structure to illustrate the physics of dislocation dissociation. (Left) fcc stacking on consecutive (1 1 1) planes. Silver, green and red atoms represent planes A, B and C, respectively. (Right) Top projection of the (1 1 1) plane shows the dissociation of a full dislocation into two partials. Such dissociation is energetically favored over slipping along b_1 due to the lowered γ_{us} in the partial directions (b_2 and b_3). (b) Comparison of the standard (unmodified) GSFE curves for pure nickel using both molecular statics (MS) and current dynamic calculation methods for the case of a full dislocation (b_1) dissociating into two Shockley partials (b_2 and b_3). (For interpretation of the references to colour in this figure legend, the reader is referred to the web version of this article.)

increase, eventually decreasing to the perfect lattice value. Then the value of γ returns to zero.

γ as a function of the reaction path coordinate computed in this study (away from the twin boundaries) is based on the geometry shown in Fig. A2a and produces the well-known baseline GSFE of the sliding half-block approach (Fig. A2b).

In order to calculate the modified GSFE due to local stress sources the tracing atoms are selected at varying proximities from the local stress source. Therefore, the stress source would contribute accordingly to the potential energy of the tracing atoms. Thus one can calculate the modified γ_{us} or the whole γ displacement plot as influenced by the stress source in that particular position. Such a technique is applied to obtain the variation of γ_{us} near the CTB during forward/reverse flow (Fig. 7c). The maximum slope calculated from such a modified whole γ displacement (as in Fig. 7a) provides τ_{max} under the influence of local stress, which is then appropriately scaled to room temperature and the lower strain rate, as explained in Appendix B.

Appendix B

Plastic flow (i.e. dislocation glide) as a function of temperature is modeled by an Arrhenius-type equation as follows [52].

$$\dot{\gamma} = \dot{\gamma}_o \exp\left(-\frac{E_a}{kT}\right) \tag{B1}$$

where E_a is the activation energy barrier, T is the absolute temperature (Kelvin), k is the Boltzmann constant, and $\dot{\gamma}_o$ is a constant associated with the rate of deformation. The derivative of E_a with respect to the glide resistant stress τ_o (a function of temperature and strain rate) provides the kinetic signature of plastic deformation, which is defined as the activation volume V^*. V^* scales with the physical area swept by the dislocations. For nanocrystalline materials or in confined volumes where there are limited dislocations sources it is of the order of several b^3, while for bulk materials its magnitude can be $1000b^3$. Its magnitude can be determined experimentally or from MD simulations. From the MD simulations the difference in flow stresses ($\Delta\tau$) for the nucleation of a single dislocation loop is calculated at two different strain rates ($\dot{\gamma}_2$ and $\dot{\gamma}_1$) and a constant temperature, using Eq. (B2) [52]:

$$V^* = -\frac{\partial E_a}{\partial \tau} = kT\frac{\partial \ln(\dot{\gamma})}{\partial \tau} = \frac{kT}{\Delta\tau}\ln\left(\frac{\dot{\gamma}_2}{\dot{\gamma}_1}\right) \tag{B2}$$

We note that E_a is a decreasing function of τ_o. Considering the linear τ_o dependence of E_a [52] one can write

$$E_a = E^* - V^*\tau_o \tag{B3}$$

Using a temperature normalization introduced by Zhu et al. [53],

$$\tau_o = \frac{E^*}{V^*} - \frac{kT}{V^*}\ln\left(\frac{kTN\upsilon_o}{\mu\dot{\gamma}V^*}\right) \tag{B4}$$

where E^* is the athermal activation energy barrier, N is the number of nucleation sites, υ_o is the attempt frequency, and μ is the shear modulus. The value of E^* is established from a knowledge of the critical stress at ~0 K and V^*. Both quantities are determined from the MD simulations conducted in this study. Then the above equation allows the determination of τ_o at different strain rates and temperatures. The constants utilized in our work are as follows: Boltzmann constant $k = 1.3806503 \times 10^{-23}$ m^2 kg s^{-2} K^{-1}; athermal activation energy barrier $E^* = 1.3$ eV; activation volume $V^* = 2.25b^3$; Burgers vector $\vec{b} = \frac{a}{6}[1\ 1\ 2]$, where lattice constant $a = 3.52$ Å; number of nucleation sites $N = 100$; attempt frequency $\upsilon_o = 3.14 \times 10^{11}$ Hz; shear

Table B1
The unstable stacking fault energy, the maximum (critical) stress for slip, and the critical stress τ_o at room temperature and typical experimental strain rates (1×10^{-4} s^{-1}).

GSFE (pure nickel)	γ_{us} (mJ m^{-2})	τ_{max} (GPa)	τ_o (GPa)
Intrinsic (unmodified)	254	6	1.8
Forward transmission	340	12.6	3.8
Reverse transmission	452	21.3	6.4

modulus $\mu = 76$ GPa; temperature $T = 300$ K (room temperature); shear strain rate $\dot{\gamma} = 1 \times 10^{-4}\ s^{-1}$. Because the MD calculations are conducted at 10 K and at high strain rates it was deemed necessary to scale the results for lower strain rates and room temperature. We note that this is still a topic of current research; the modifications made above and illustrated in Table B1 represent the current state of knowledge. Future refinements in this area will not, however, change the conclusions reached in this work.

The intrinsic (unmodified) γ_{us} in Table B1 corresponds to the unstable stacking fault energy of pure Ni. The modified γ_{us} levels in Table B1 are for a dislocation within the twin boundary zone, as explained in the text. The corresponding critical stress levels are encountered during forward/reverse transmission, as shown in Fig. 7c. The τ_{max} values are obtained from the slope of the γ displacement curves from the simulations. The third column is obtained from Eq. (B4).

References

[1] ASME. Criteria of the ASME boiler and pressure vessel code for design by analysis in Sections III and VIII, Division 2. New York: ASME; 2010.
[2] Asaro RJ, Suresh S. Acta Mater 2005;53:3369–82.
[3] Deng C, Sansoz F. Acta Mater 2009;57:6090–101.
[4] Lu L, Schwaiger R, Shan ZW, Dao M, Lu K, Suresh S. Acta Mater 2005;53:2169.
[5] Singh A, Tang L, Dao M, Lu L, Suresh S. Acta Mater 2011;59:2437.
[6] Wu ZX, Zhang YW, Srolovitz DJ. Acta Mater 2009;57:4508.
[7] Zhu T, Li J, Samanta A, Kim HG, Suresh S. Proc Natl Acad Sci USA 2007;104:3031–6.
[8] Zhao Y, Zhu Y, Lavernia EJ. Adv Eng Mater 2010;12:769–78.
[9] Zhong S, Koch T, Wang M, Scherer T, Walheim S, Hahn H, et al. Small 2009;5:2265–70.
[10] Zhu YT, Narayan J, Hirth JP, Mahajan S, Wu XL, Liao XZ. Acta Mater 2009;57:3763–70.
[11] Kumar KS, Van Swygenhoven H, Suresh S. Acta Mater 2003;51:5743.
[12] Lu K, Lu L, Suresh S. Science 2009;324:349–52.
[13] Lu L, Shen Y, Chen X, Qian L, Lu K. Science 2004;304:422–6.
[14] Weertman JR. Mater Sci Eng A 1993;166:161–7.
[15] Conrad H, Narayan J. Scripta Mater 2000;42:1025–30.
[16] Boyce B, Padilla H. Metal Mater Trans A 2011;42:1793.
[17] Hanlon T, Kwon YN, Suresh S. Scripta Mater 2003;49:675.
[18] Hanlon T, Tabachnikova ED, Suresh S. Int J Fatigue 2005;27:1147.
[19] Padilla H, Boyce B. Exp Mech 2009;50:5.
[20] Xie J, Wu X, Hong Y. Scripta Mater 2007;57:5.
[21] Sangid MD, Pataky GJ, Sehitoglu H, Rateick RG, Niendorf T, Maier HJ. Acta Mater 2011;59:7340.
[22] Boettner, McEvily, Liu. Philos Mag 1964;10:95.
[23] Forsyth PJE. Acta Metal 1963;11:703.
[24] McClintock FA. In: Drucker DC, Gilman JJ, editors. Fracture of Solids. London: Gordon & Breach Science Publishers, 1963, p. 65.
[25] Neumann P. Acta Metal 1969;17:1219.
[26] Neumann P. Acta Metal 1974;22:1167.
[27] Pippan R. The dislocation-free zone and the threshold of the effective stress intensity range. Elmsford (NY): Pergamon Press; 1989.
[28] Pippan R. Acta Metal Mater 1991;39:255.
[29] Pippan R. Int J Fracture 1992;58:305.
[30] Riemelmoser F, Pippan R, Stuwe H. Int J Fracture 1997;85:157.
[31] Ezaz T, Sangid MD, Sehitoglu H. Philos Mag 2011;91:1464.
[32] Hartley CS, Blachon DLA. J Appl Phys 1978;49:4788.
[33] Cai W, Bulatov VV, Chang J, Li J, Yip S. In: Nabarro FRN, Hirth JP, editors. Dislocations in solids. Amsterdam: Elsevier; 2005. p. 1.
[34] Frenkel D, Smit B. Understanding molecular simulation: from algorithms to applications. New York: Academic Press; 2001.
[35] Tadmor EB, Miller RE. Modeling materials – continuum, atomistic and multiscale techniques. Cambridge: Cambridge University Press; 2011.
[36] Farkas D, Willemann M, Hyde B. Phys Rev Lett 2005;94:165502.
[37] Nishimura K, Miyazaki N. Comput Mater Sci 2004;31:269.
[38] Potirniche GP, Horstemeyer MF, Gullett PM, Jelinek B. Proc Roy Soc Lond A Math Phys Eng Sci 2006;462:3707–31.
[39] Plimpton S. J Comput Phys 1995;117:1–19.
[40] Humphrey W, Dalke A, Schulten K. J Molec Graphics 1996;14:33–8.
[41] Li J. Modeling Simul Mater Sci Eng 2003;11:173.
[42] Zhou M. Proc Roy Soc Lond A Math Phys Eng Sci 2003;459:2347–92.
[43] Foiles SM, Hoyt JJ. Acta Mater 2006;54:3351.
[44] Vitek V. Philos Mag 1968;18:773.
[45] Mahajan S, Chin GY. Acta Metal 1973;21:173.
[46] Jin ZH, Gumbsch P, Ma E, Albe K, Lu K, Hahn H, et al. Scripta Mater 2006;54:1163.
[47] Kumar KS, Suresh S, Chisholm MF, Horton JA, Wang P. Acta Mater 2003;51:387.
[48] Yang Y, Imasogie B, Fan GJ, Liaw PK, Soboyejo WO. Metal Mater Trans A 2008;39:1145.
[49] Christian JW, Mahajan S. Prog Mater Sci 1995;39:1.
[50] Mughrabi H. Metal Mater Trans A 2009;40:1257.
[51] Hirth JP, Lothe J. Theory of dislocations. New York: McGraw-Hill; 1967. p. 780.
[52] Conrad H, Frederick S. Acta Metal 1962;10:1013.
[53] Zhu T, Li J, Samanta A, Leach A, Gall K. Phys Rev Lett 2008;100:025502.